This PDF file includes:

Supplementary text

Figures S1 to S7

Tables S1 to S2

Legends for Movie S1

SI References

Other supplementary materials for this manuscript include the following:

Movie S1

$$V_{total} = \int_0^R \int_{D(r)}^H \int_0^{2\pi} r d\theta dr dz$$

$$V_{shallow}(t) = \int_{r_{int}(t)}^R \int_{D(r)}^H \int_0^{2\pi} r d\theta dr dz$$

$$A_{shallow}(t) = \pi(R^2 - r_{int}^2(t))$$

$$A_{total} = \pi R^2$$

If $Ro_R < L_{shallow}$

$$V_{total}(t) = \int_0^{r_{int}(t)+Ro_R(t)} \int_{D(r)}^H \int_0^{2\pi} r d\theta dr dz$$

$$V_{shallow}(t) = \int_{r_{int}(t)}^{r_{int}(t)+Ro_R(t)} \int_{D(r)}^H \int_0^{2\pi} r d\theta dr dz$$

$$A_{shallow}(t) = \pi((r_{int}(t) + Ro_R(t))^2 - r_{int}^2(t))$$

$$A_{total}(t) = \pi(r_{int}(t) + Ro_R(t))^2$$

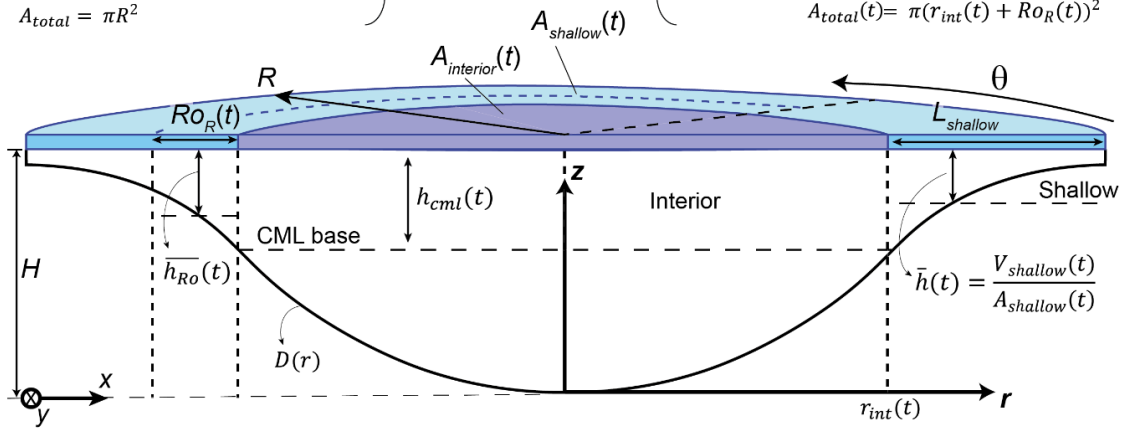

$$D(r) = H - \frac{H - d_{min}}{2}\left(1 - tanh\frac{r - r_0}{\beta}\right)$$

$$G(t) \equiv \left|\left\{1 - \left(\frac{r_{int}(t)}{R}\right)^2\right\}\left\{\frac{\bar{h}(t)}{h_{cml}(t)} - 1\right\}\right|$$

$$G(t) \equiv \left|\frac{A_{shallow}}{A_{total}}\left(\frac{\bar{h}}{h_{cml}} - 1\right)\right|$$

$$G_{Ro}(t) \equiv \left|\left\{1 - \left(\frac{r_{int}(t)}{r_{int}(t) + Ro_R(t)}\right)^2\right\}\left\{\frac{\overline{h_{Ro}}(t)}{h_{cml}(t)} - 1\right\}\right|$$

Figure S1: Schematic of volumes, areas and relevant length scales. Half of the three-dimensional basin. (t) = time-dependent variables; (r) = radial-dependent variables.

S1. Supplementary Information Text

S1.1 Calculation of the Rossby number.

Eq. (4) was used to calculate *Ro*. The shallow littoral region is time dependent and it was calculated as the water columns where $D < h_{cml}$ (see Fig. S1). $U_{rs\text{-max}}$ was then calculated as the maximum radial velocity within this region. $U_{rs\text{-max}}$ was smoothed over 2h to remove the high frequency fluctuations in the signal (Fig. S2a). The smoothed $U_{rs\text{-max}}$ signal was used to calculate the Rossby radius ($Ro_R = U_{rs\text{-max}} / f$, Fig. S2b) and the Rossby number (Eq. (4), Fig. S2c).

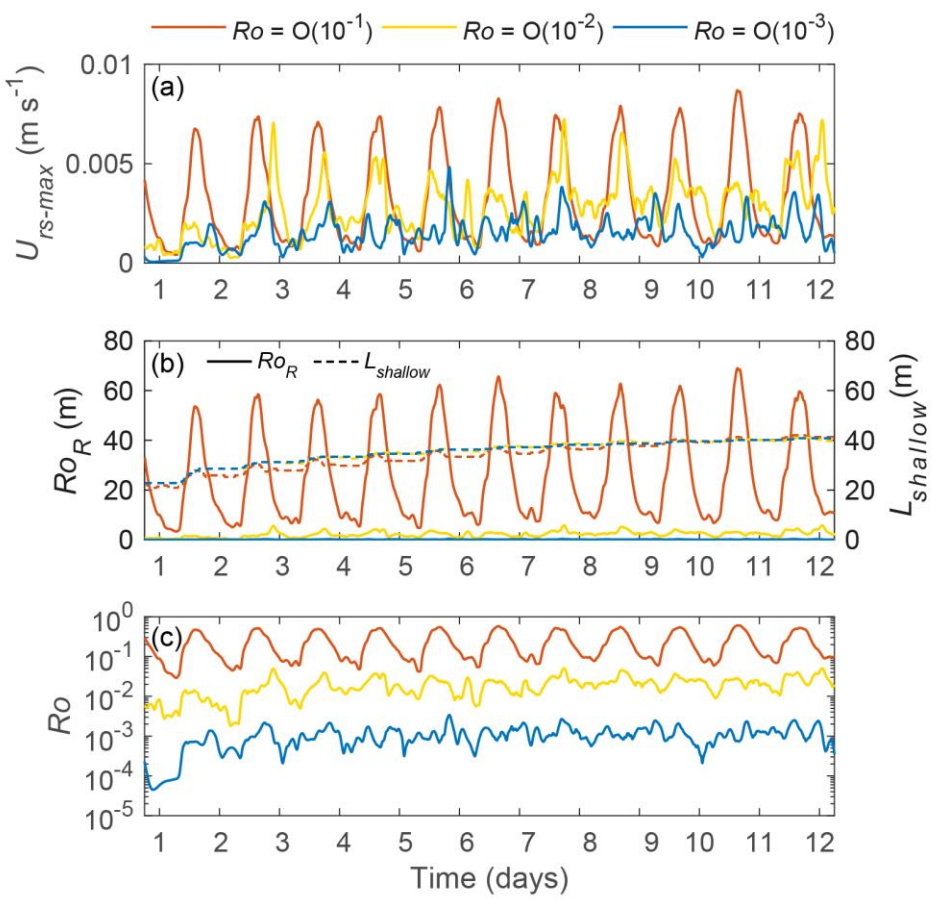

Figure S2: Rossby number. Time evolution of (a) maximum radial velocity in the littoral region, (b) Rossby radius and $L_{shallow}$, and (c) Rossby number. 2h-averaged signals.

S1.2 Geostrophy test.

Once a geostrophic balance is set, the Coriolis acceleration balances the horizontal pressure-gradient acceleration, and azimuthal velocities, assuming steady state, can be estimated by Eq. (S1).

$$u_\theta = \frac{1}{f\rho_0}\frac{\partial P}{\partial r}\,. \tag{S1}$$

Here P is pressure. To test for geostrophy, modeled azimuthal velocities within the CML are compared with estimates from Eq. (S1) for runs 1-3 in Table 1. Figure S3a shows that the modeled azimuthal velocities in the runs with *Ro* O(10^{-3}–10^{-2}) closely follow the 1:1 relationship (black dotted line in Fig. S3a) indicating that geostrophy is achieved. The spreading of values around the 1:1 line is however larger for the transitional regime, *Ro* O(10^{-2}). For the *Ro* O(10^{-1}) case, Eq. (S1) failed to predict modeled azimuthal velocities (note the deviation of the red dots from the 1:1 relationship in Fig. S3a), confirming that the flow is ageostrophic. The two different regimes for *Ro* O(10^{-1}) and *Ro* O(10^{-3}–10^{-2}) are further confirmed in Fig. S3b, showing the root mean square differences, RMSD, between modeled and estimated (Eq. (S1)) azimuthal velocities.

For *Ro* O(10^{-1}), Eq. (S1) overpredicted the strength of the gyres, that is the magnitude of the azimuthal velocities. By adding the centripetal acceleration to the steady-state balance (Eq. (S2)), the spreading of values around the 1:1 line decreases indicating that a cyclogeostrophic balance is set in this scenario

$$\frac{u_\theta^2}{r} + fu_\theta - \frac{1}{\rho_0}\frac{\partial P}{\partial r} = 0 \tag{S2}$$

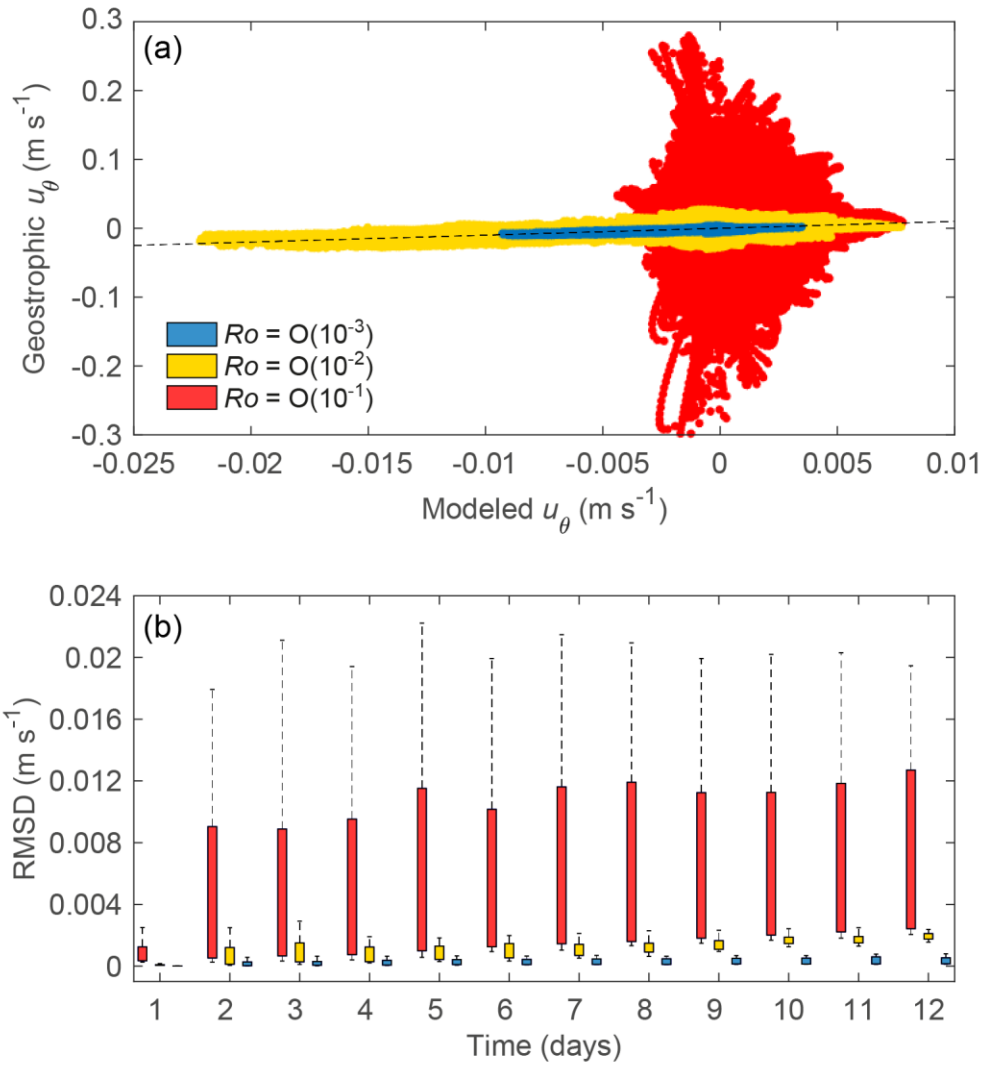

Figure S3: Test for geostrophy. (a) Modeled azimuthal velocities within the CML *vs.* those predicted by Eq. (S1) (geostrophic balance) and (b) Root mean square differences, RMSD, between the two for the different simulated days. The black dotted line in (c) corresponds to the 1:1 relationship. Colored bars in (b) show the interquartile range.

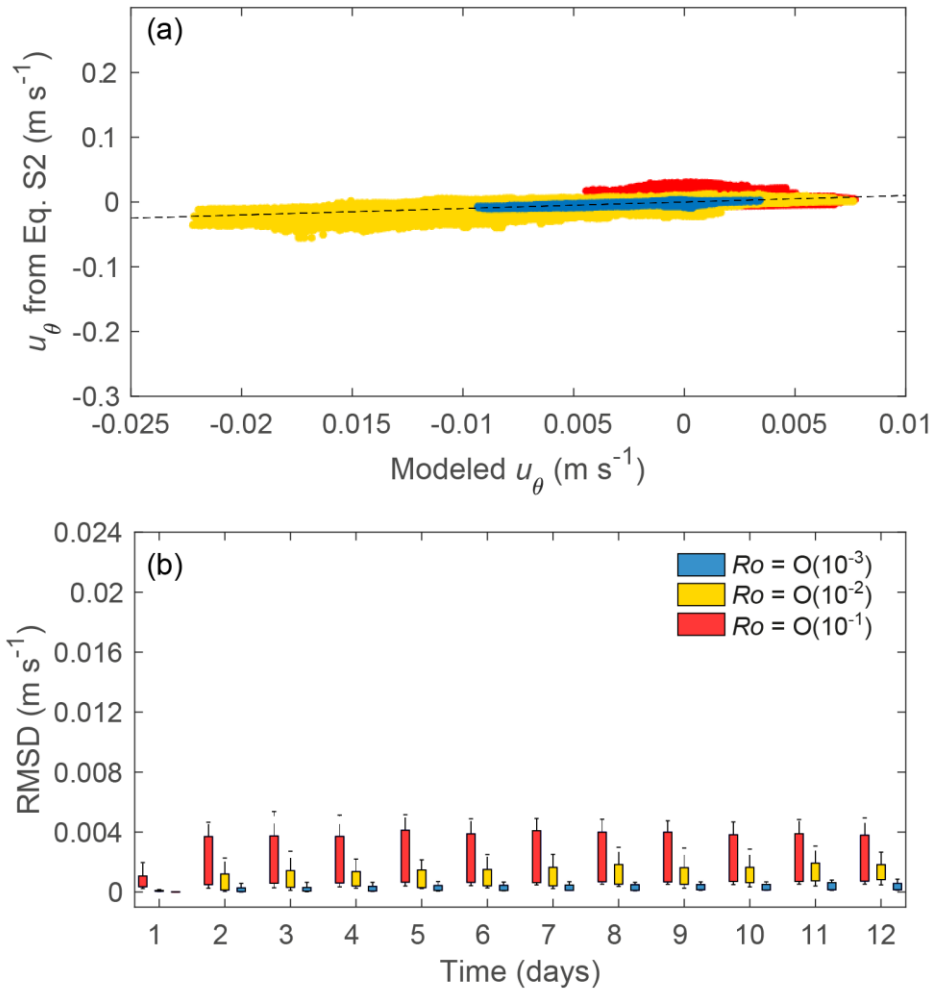

Figure S4: Test for cyclogeostrophy. (a) Modeled azimuthal velocities within the CML *vs.* those predicted by Eq. (S2) (cyclogeostrophic balance) and (b) Root mean square differences, RMSD, between the two for the different simulated days. The black dotted line in (a) corresponds to the 1:1 relationship. Colored bars in (b) show the interquartile range.

S1.3 Geometrical factor G_{Ro}.

Taking the flushing littoral region as the region within a Rossby radius from the lake interior when $Ro_R < L_{shallow}$, the surface area of the littoral region in our bathymetry with a circular surface area, is defined as $A_{shallow} = 2\pi(r_{int}+Ro_R)^2-2\pi r_{int}^2$, where $r_{int} = R - L_{shallow}$ (Fig. S1). The total area, A_{total}, is now equal to $2\pi(r_{int}+Ro_R)^2$ (Fig. S1). Eq. (1) can be then rewritten to obtain Eq. (9) as:

$$G_{Ro} = \left|\left(\frac{\pi(r_{int} + Ro_R)^2 - \pi r_{int}^2}{\pi(r_{int} + Ro_R)^2}\right)\left(\frac{\overline{h_{Ro}}}{h_{cml}} - 1\right)\right| = \left|\left(1 - \frac{r_{int}^2}{(r_{int} + Ro_R)^2}\right)\left(\frac{\overline{h_{Ro}}}{h_{cml}} - 1\right)\right| =$$

$$= \left|\left(1 - \frac{(R - L_{shallow})^2}{(R - L_{shallow} + Ro_R)^2}\right)\left(\frac{\overline{h_{Ro}}}{h_{cml}} - 1\right)\right|, \qquad \text{(S3)}$$

where the average depth of the littoral region from $R_{interior}$ to $R_{interior}+Ro_R$ is referred to as $\overline{h_{Ro}}$ (Fig. S1). For the calculations of G_{Ro}, we used the maximum Ro_R achieved each daily cycle in Fig. S2b, which represents the maximum radial extension of a gravity current in a given day. Note that the maximum Ro_R is less than $L_{shallow}$ (Fig. S2b) only for *Ro* O(10^{-2}-10^{-3}).

S1.4 Calculations of the latitudinal range of variability of *Ro* for radiatively-driven circulation under ice in lakes on Earth.

For the calculations in Figs. 5d-e, the publicly available HydroLAKES database (Messager et al., 2016; http://www.hydrosheds.org) was used. This database includes information for ~1.4 million lakes around the globe with surface areas ≥ 10 Ha. There is no information about the freezing regime (if existing) of lakes in this database, which prevented us from limiting the analysis to only those lakes that actually freeze. Instead, our analysis provides the range for potential Rossby numbers based on the distribution of lakes over the globe in terms of their size and latitude. We discarded the large lakes with surface area > 10^4 km^2, that tend to cover several degrees in latitude, from the analysis and we also discarded lakes in latitudes lower than 30°, which is the lower limit for lakes that freeze in the Himalayas and the Tibet Plateau. Order of magnitude estimates of *Ro* were made as follows:

1. We calculated the Coriolis frequency based on the latitudinal information of the lake pour point (variable "*Pour_lat*") as $f = 2\Omega \sin(\varphi)$, where Ω ($\approx 7.29 \times 10^{-5}$ rad s^{-1}) is the angular velocity of the Earth around its axis and φ the latitude. Absolute values were used, so no distinction was made between lakes located in the northern and southern hemisphere.
2. For the characteristic length, we took, for each lake, the radius of a circle with the same surface area (variable "*Lake_area"*) of the lake. Given that the circular shape is a strong assumption, we further discarded lakes whose shoreline

development (variable "*Shore_dev*") is > 2 (see details in http://www.hydrosheds.org).

3. For the characteristic velocities we used two values per lake, varying by an order of magnitude: 0.005 and 0.05 m s^{-1}, consistent with the reported O (10^{-3}–10^{-2}) m s^{-1} radial velocities under ice (Forrest et al., 2013; Kirillin et al., 2015; Rizk et al., 2014).

A total of 1040034 lakes were finally selected, each yielding two values of *Ro*.

S1.5 Model calibration and validation.

It is challenging to estimate from the field the exact contribution of the different forcing mechanisms at play, which complicates the validation of a RANS model for a specific process, such as differential heating driven by radiatively-driven convection under the ice. The spectral LES of Ulloa et al. (2019) offer, thus, a unique opportunity, allowing for a precise evaluation of the rate of heating and cross-shore transport, resulting from this process alone. MITgcm was calibrated against those simulations. Since our simulations build upon theirs, their boundary conditions and radiative forcing are the same as those presented in Methods, except for their bathymetry, which was two dimensional and given by Eq. (2) in the x-direction, but expanded only 1-m in the y-direction. MITgcm was used to reproduce the 2D LES and we used the evolution of temperature at the CML, T_{cml}, as the variable of calibration (Tables S1-S2). For the model validation, we focused on the time evolution of variables that were critical for the dynamics of the CML, that is h_{cml}, the root-mean-square velocities in the CML $U_{rms\text{-}cml}$, and the ratio Φ_{ra}/Φ_r (Table S2). Φ_{ra}/Φ_r accounts for the proportion of the radiative heating that is actually converted to kinetic energy, and, thus, the proportion that drives the fluid into motion (details in Ulloa et al., 2019; Winters et al., 2019). The first 20 radiative cycles were used for calibration purposes while the best simulation was extended until 28 cycles as in Ulloa et al. (2019) for validation purposes. As calibrating parameters for the model, we used the background grid-dependent lateral viscosities, the 3D Smagorinsky coefficient and the horizontal Laplacian diffusion of heat K_h. These parameters take the name of *AhvisGrid*, *smag3D_coeff* and *diffKhT* in the MITgcm code, respectively, and were allowed to vary up to three orders of magnitude (Table S1). Background vertical diffusivities and

viscosities, K_z and υ_z, were held constant in all simulations and equal to molecular values (see Sect. 2).

Table S1: Calibration of MITgcm. Model runs, calibration parameters and root mean square errors (RMSE) and linear-fit correlation coefficients for T_{cml} after 20 radiative cycles.

run	*AhvisGrid*	*diffKhT** (m^2 s^{-1})	*smag3D_coeff*	RMSE (°C)	R^2
2D_1	5×10^{-3}	1×10^{-4}	5×10^{-4}	0.0053	0.9999
2D_2	5×10^{-3}	1×10^{-5}	5×10^{-4}	0.0067	0.9999
2D_3	2×10^{-3}	1×10^{-5}	5×10^{-4}	0.0039	0.9999
2D_4	2×10^{-3}	1×10^{-4}	5×10^{-4}	0.0043	0.9999
2D_5	2×10^{-3}	1×10^{-3}	5×10^{-4}	0.0152	0.9999
2D_6	2×10^{-3}	1×10^{-5}	5×10^{-2}	0.0111	0.9998
2D_7	6×10^{-4}	1×10^{-5}	5×10^{-4}	0.0068	0.9998
2D_8	6×10^{-4}	1×10^{-4}	5×10^{-4}	0.0074	0.9989
2D_9	2.5×10^{-4}	1×10^{-5}	5×10^{-4}	0.0169	0.9998
2D_10	2.5×10^{-4}	1×10^{-3}	5×10^{-4}	0.0191	0.9995
2D_11	2.5×10^{-4}	1×10^{-5}	5×10^{-3}	0.0144	0.9998
2D_12	2.5×10^{-4}	1×10^{-4}	5×10^{-3}	0.0153	0.9998
2D_13	2.5×10^{-4}	1×10^{-3}	5×10^{-3}	0.0204	0.9995
2D_14	2.5×10^{-4}	1×10^{-5}	5×10^{-2}	0.0149	0.9998

Table S2: Calibration/validation of MITgcm. Variables used and root mean square errors (RMSE) and linear-fit correlation coefficients for run 2D_3 in Table S1 after 28 radiative cycles.

Variable	Description	Units	Purpose	RMSE	R^2
T_{cml}	Temperature of the CML at the lake interior	°C	Calibration	0.008°C	0.999
h_{cml}	Depth of the CML at the lake interior	m	Validation	0.54 m	0.996
$U_{rms\text{-}cml}$	Root-mean-square velocity in the CML	m s^{-1}	Validation	7×10^{-4} m s^{-1}	0.530
Φ_{ra} / Φ_r	Ratio of available to total solar energy supply rate	-	Validation	0.012	0.931

All simulations show high correlation coefficients ($R^2 > 0.998$) for T_{cml} and the best simulation—based on the lowest RMSE value— was run 2D_3 with an RMSE error of $O(10^{-3})$°C (Table S1). This error represents less than 1% of the temperature increase of

T_{cml} during the 20 radiative cycles. The time evolution of T_{cml} and temperature profiles at the lake interior and their comparison with the results from spectral LES for the total 28 radiative cycles are shown in Fig. S5 (note that, in comparison to Table S1, the RMSE values displayed in this figure and in Table S2 now cover the 28 radiative cycles).

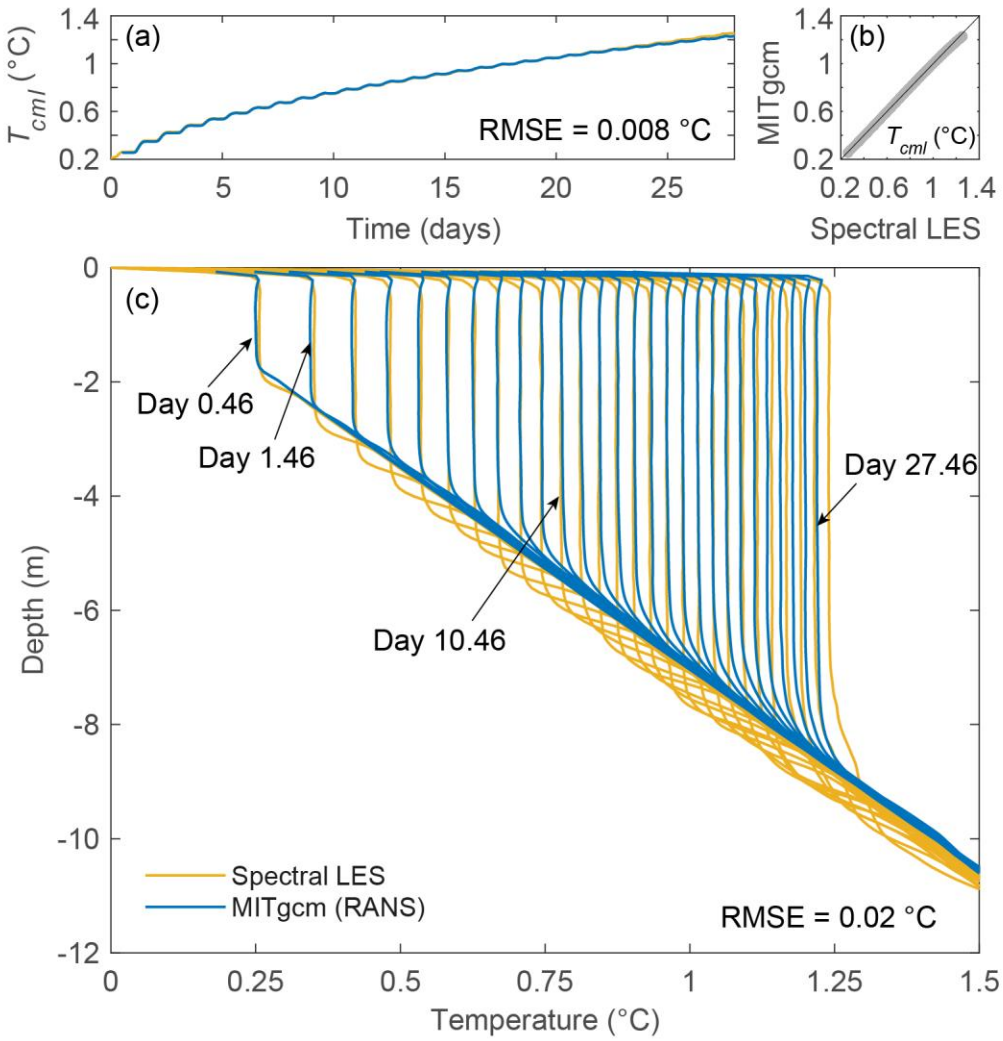

Figure S5: Temporal evolution of temperature at the lake interior. (a) Evolution in time and (b) one-to-one comparisons for T_{cml}. (c) Time evolution of temperature profiles at the lake interior. Black lines in (b) show the 1:1 relationship. RMSE values in (a,c) refer to the 28 cycle period. Comparison between MITgcm and spectral LES (Ulloa et al., 2019).

The best simulation after the calibration for the evolution of T_{cml} (run 2D_3 in Tables S1-S2) was also able to satisfactorily reproduce the evolution of the variables used for the

model validation, especially for h_{cml} and Φ_{ra}/Φ_r, with low RMSE values and high correlation coefficients ($R^2 > 0.99$) (Table S2). The average ~0.5m underestimation in the h_{cml} values (Fig.S5a) is the result of convective cells in MITgcm not being able to create the depression of the isotherms at the base of the CML (Fig. S5). Although $U_{rms\text{-}cml}$ is reproduced less satisfactorily by MITgcm (Fig. S6b, S6e), this was to be expected given the order of magnitude for this variable, O (10^{-3}) m s^{-1}. Still, MITgcm is able to reasonably reproduce both the magnitudes and the amplitudes in the $U_{rms\text{-}cml}$ signal.

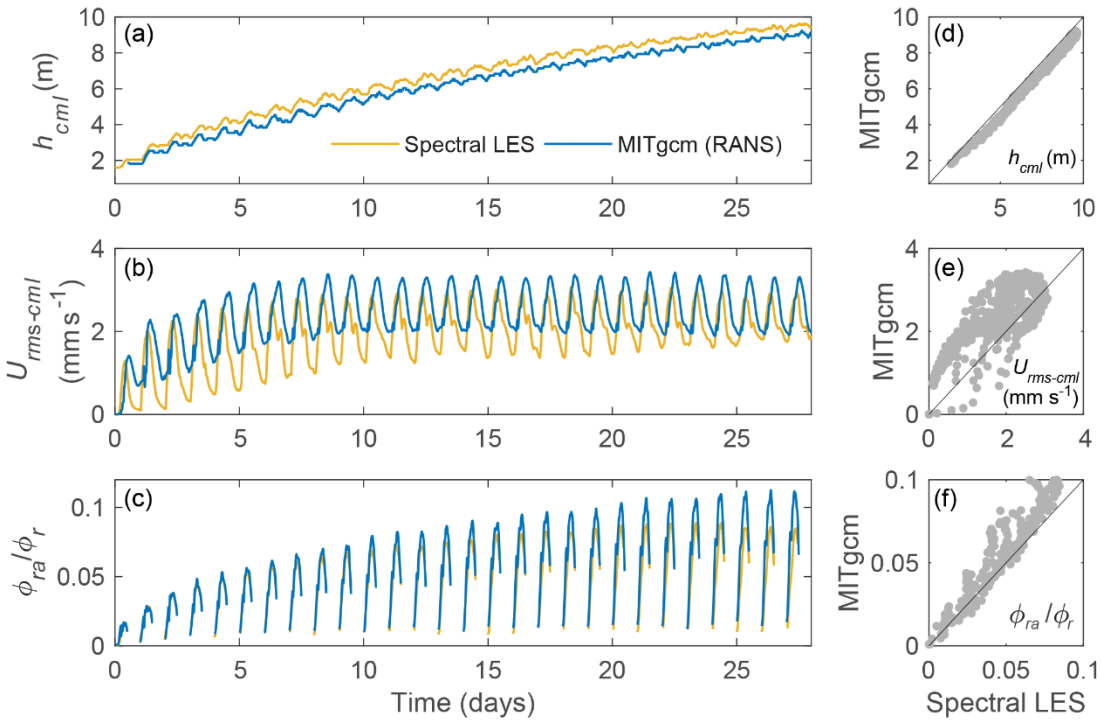

Figure S6: Model validation. (a-c) Evolution in time and (d-f) one-to-one comparisons of the model-validation variables in Table S2. Black lines in (d-e) show the 1:1 relationship. Comparison between MITgcm and spectral LES (Ulloa et al., 2019).

To test the influence of the resolution of the grid in model solutions, the basin was discretized using grid cells of different size in the horizontal. An increase in horizontal grid size of 2 m (l_x = 2 m) was used. Grid cells of size Δx = 2 m, 4 m and 6 m were tested, together with the Δx = 0.9 m. To analyze convergence, we calculated the error E (Eq. (S3)), expressed as the L2 norm of the difference (e.g. Fringer et al., 2006) between solutions with the different grids and that with the higher resolution grid (Δx = 0.9 m)

$$E = \frac{\sum_{p=1}^{N}(\chi-\chi_{ref})^2}{\sum_{p=1}^{N}(\chi_{ref})^2} \quad \text{(S4)}$$

where χ is either T_{cml}, h_{cml}, $U_{rms\text{-}cml}$ or Φ_{ra} / Φ_r in each point p of the time series, with a total of N points, and the subscript *ref* refers to the results with the 0.9m-resolution grid. As the grid resolution increases, errors tend to converge from O(l_x) to accuracy O(l_x^2) accuracy, except for h_{cml}, which remains O(l_x) (Fig. S7). Errors in the 2m resolution grid are less than 2% for all four variables (Fig. S7), which suggests grid convergence.

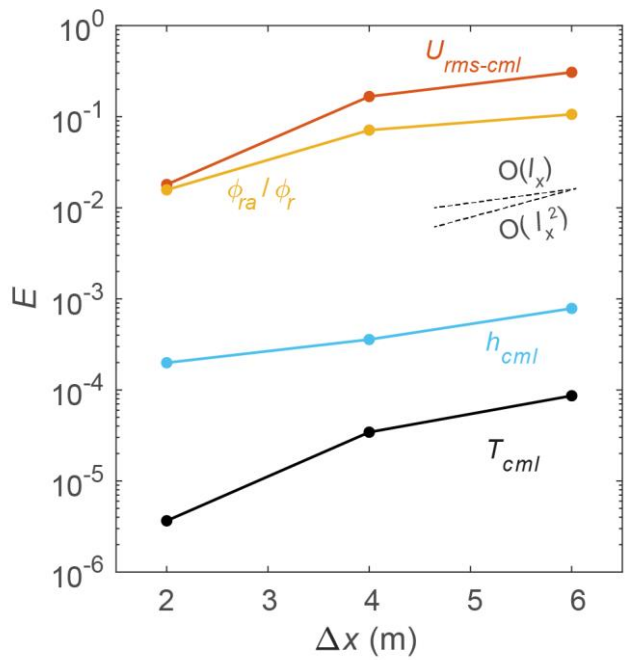

Figure S7: Grid convergence. L2 norm error *E* (Eq. (S4)) after 20 radiative cycles for different horizontal-grid resolutions and variables in Table S1.

Movie S1 (separate file).

Daily evolution of the simulated cross-sectional temperature (0.02°C isotherm spacing), radial and azimuthal velocities (0.002 m s^{-1} isovel spacing), and of the depth-averaged

azimuthal velocities and flow streamlines at depths ≤ h_{cml}. Radial and azimuthal velocities are positive towards the lake interior and for cyclonic circulation, respectively.

SI References

Forrest, A. L., Laval, B. E., Pieters, R. and S. S. Lim, D.: A cyclonic gyre in an ice-covered lake, Limnol. Oceanogr., 58(1), 363–375, doi:10.4319/lo.2013.58.1.0363, 2013.

Fringer, O. B., Gerritsen, M. and Street, R. L.: An unstructured-grid, finite-volume, nonhydrostatic, parallel coastal ocean simulator, Ocean Model., 14(3–4), 139–173, doi:http://dx.doi.org/10.1016/j.ocemod.2006.03.006, 2006.

Kirillin, G. B., Forrest, A. L., Graves, K. E., Fischer, A., Engelhardt, C. and Laval, B. E.: Axisymmetric circulation driven by marginal heating in ice-covered lakes, Geophys. Res. Lett., 42(8), 2893–2900, doi:10.1002/2014GL062180, 2015.

Messager, M. L., Lehner, B., Grill, G., Nedeva, I. and Schmitt, O.: Estimating the volume and age of water stored in global lakes using a geo-statistical approach, Nat. Commun., 7(1), 1–11, doi:10.1038/ncomms13603, 2016.

Rizk, W., Kirillin, G. and Leppäranta, M.: Basin-scale circulation and heat fluxes in ice-covered lakes, Limnol. Oceanogr., 59(2), 445–464, doi:10.4319/lo.2014.59.2.0445, 2014.

Ulloa, H. N., Winters, K. B., Wüest, A. and Bouffard, D.: Differential Heating Drives Downslope Flows that Accelerate Mixed-Layer Warming in Ice-Covered Waters, Geophys. Res. Lett., 46(23), 13872–13882, doi:10.1029/2019GL085258, 2019.

Winters, K. B., Ulloa, H. N., Wüest, A. and Bouffard, D.: Energetics of radiatively-heated ice-covered lakes, Geophys. Res. Lett., 2019GL084182, doi:10.1029/2019GL084182, 2019.